CHEMISTRY OF MATERIALS

pubs.acs.org/cm

Article

Br-Induced Suppression of Low-Temperature Phase Transitions in Mixed-Cation Mixed-Halide Perovskites

Juanita Hidalgo, Joachim Breternitz, Daniel M. Többens, Diana K. LaFollette, Charles N. B. Pedorella, Meng-Ju Sher, Susan Schorr,* and Juan-Pablo Correa-Baena*

Cite This: *Chem. Mater.* 2024, 36, 10167−10175

Read Online

ACCESS | Metrics & More | Article Recommendations | Supporting Information

ABSTRACT: Mixed-cation mixed-halide lead perovskites have been shown to be excellent candidates for solar energy conversion. However, understanding the structural phases of these mixed-ion perovskites across a wide range of operating temperatures, including very low temperatures for space applications, is crucial. In this study, we investigated the structure of formamidinium-based $Cs_yFA_{1-y}Pb(Br_xI_{1-x})_3$ using low-temperature in situ synchrotron powder X-ray diffraction. Our findings revealed that substituting the I anion with Br in mixed-cation (Cs,FA) perovskites suppressed the phase transformation from tetragonal to orthorhombic at low temperatures. The addition of Br also prevented the formation of nonperovskite secondary phases. We gained fundamental insights into the structural behavior of these materials by creating a low-temperature phase diagram for the compositional set of mixed-cation mixed-halides. This understanding of the structural properties lays the groundwork for designing more robust and efficient energy materials capable of functioning under extreme temperature conditions, including space-based solar energy conversion.

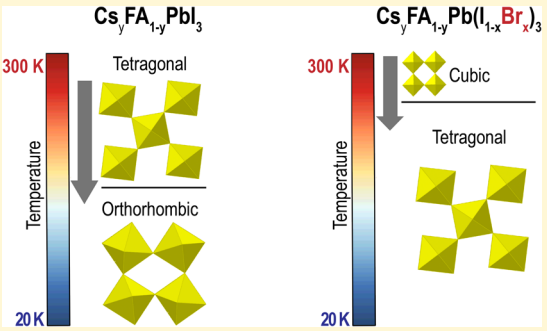

INTRODUCTION

Mixed-cation mixed-halide lead halide perovskites (LHP) have emerged as promising materials for solar energy conversion.[1] Specifically, formamidinium (FA)-rich compositions have demonstrated higher thermal stability and an optimal bandgap for single-junction solar cells.[2] Compositional mixing has been employed to achieve optimal optoelectronic properties and stability.[3,4] However, it is crucial to unravel the structural phases across a wide range of operating temperatures, including very low temperatures relevant to space applications, to ensure the proper functioning and stability of these materials. The most common and efficient compositions include mixing cesium (Cs) and FA in the A-site as well as iodine (I) and bromine (Br) in the X-site, resulting in $(Cs,FA)Pb(I,Br)_3$ LHP compositions. A knowledge gap exists on a complete phase diagram for both mixed-cation and mixed-halide compositions. In this work, we aim to construct a low-temperature phase diagram for (Cs,FA) mixed halide (I,Br) perovskites.

Previous studies have reported low-temperature phase diagrams for single-ion compositions such as $FAPbI_3$,[5] $CsPbI_3$,[6] $FAPbBr_3$,[7] and $CsPbBr_3$.[8] Generally, perovskites exhibit a cubic (α) phase at high temperatures above a certain threshold. As the temperature decreases, the perovskite structure undergoes phase transitions from cubic to tetragonal (β) and then from tetragonal to orthorhombic (γ) phase. Phase diagrams have also been studied for single-cation/mixed-halide or mixed-cation/single-halide compositions. For instance, Lehmann et al. investigated and presented the temperature phase diagram for $MAPb(I,Br)_3$ compositions, highlighting the two phase transitions.[9] Nasstrom et al. reported the high-temperature phase diagram for $CsPb(I,Br)_3$, observing different phase transitions during heating and cooling.[10] Other studies focused on the phase diagram for the mixed-cation iodide-based perovskites, either (MA,FA)-PbI_3[11] or $(Cs,FA)PbI_3$.[12,13] In the first,[11] they used Raman spectroscopy and photoluminescence to uncover different low-temperature phase transitions dependent on the FA content, related to its higher symmetry compared to MA. In the latter, for (Cs,FA) perovskite, the authors revealed the cubic-tetragonal-orthorhombic transitions and solubility limit of the Cs/FA ratio to form a pure perovskite phase.[12,13]

In the case of pure Br-based compositions, it has been demonstrated that Cs substitution in $FAPbBr_3$ perovskite suppresses the orthorhombic phase transition at low temperatures, attributed to a geometric blocking associated with the rotation of FA molecules.[14] The suppression of the

Received: June 14, 2024
Revised: September 27, 2024
Accepted: September 30, 2024
Published: October 4, 2024

orthorhombic phase at low temperatures has also been observed in mixed-cation MA-dimethylammonium (DMA) lead bromide perovskites (MA,DMA)$PbBr_3$.[15,16] This suppression was attributed to the increased disorder of the organic cations in the mixed samples, leading to higher symmetry and less distortion of the inorganic framework. The improved structural stability also enhanced their photodetection capabilities.[16] Despite the knowledge from studying low-temperature phase transitions in various cation and halide combinations, a complete structural phase diagram for widely used and highly efficient LHPs $(Cs,FA)Pb(I,Br)_3$ is still lacking.

Herein, we study the crystal structure of FA-based LHP compositions $Cs_yFA_{1-y}Pb(Br_xI_{1-x})_3$ by low-temperature in situ synchrotron powder X-ray diffraction (XRD) from 300 to 23 K. Our focus was on FA-rich and I-rich compositions to maintain a low bandgap suitable for single-junction solar cells. Our findings reveal that the low-temperature orthorhombic phase transition is suppressed as Br replaces I in the mixed-cation LHP compositions. Additionally, the inclusion of Br eliminates secondary nonperovskite phases. We construct three halide-dependent temperature phase diagrams for different Cs concentrations, demonstrating that adding Br to the mixed-cation (Cs,FA) system stabilizes the higher-symmetry perovskite structure from room to low temperatures and prevents the formation of nonperovskite phases. This fundamental understanding of the perovskite structure in a wide range of temperatures provides a basis for designing and developing more resilient and efficient materials capable of functioning under extreme conditions. Comprehending the state-of-the-art halide perovskite's structure across the entire temperature range is paramount.

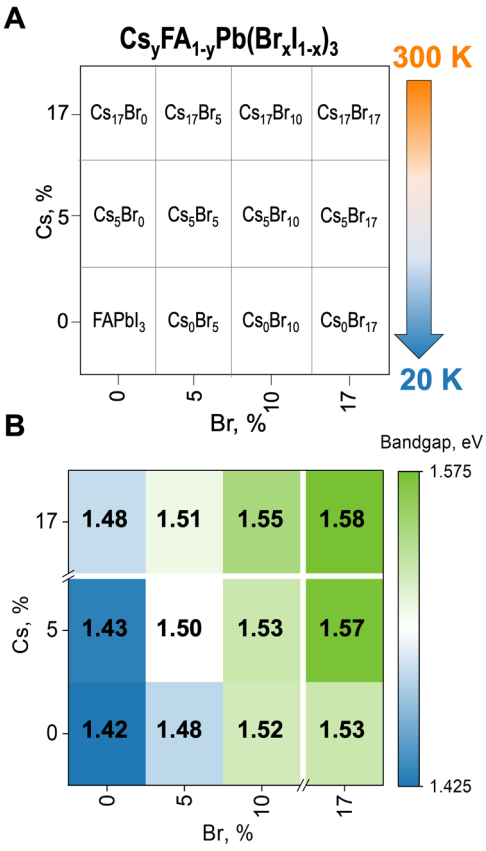

Figure 1. Mixed-cation and mixed-halide perovskite compositions of study. (A) Selected compositions to study the in situ phase transitions from 300 to 23 K and (B) bandgap from UV−vis at room temperature.

RESULTS AND DISCUSSION

Properties and Structure at Room Temperature and 300 K. To investigate the low-temperature phase transitions for different FA-based LHP compositions, we selected a mixed-cation and mixed-halide compositional space $Cs_yFA_{1-y}Pb(Br_xI_{1-x})_3$, as shown in Figure 1A. We chose this compositional space to have FA-rich compositions with ideal bandgaps for single-junction solar cells.[2,5,17] The selected upper limit for Cs was 17% molar, given that its thermodynamic limit to form a single-phase perovskite when mixed with FA is around 15[12,13,18] and 20% molar.[19] Therefore, we chose 17%, targeting a single-phase perovskite formation. The upper limit chosen for Br was 17%, keeping an I-based composition and equaling the maximum added percent of Cs.

Bandgap tunability is one of the main advantages of LHPs.[20] To analyze the optoelectronic properties of the synthesized materials, we measured UV−vis absorption spectroscopy (at room temperature) and used the Tauc-plot method (Figure S1) to calculate the optical bandgap.[21] In Figure 1B, the lowest experimental bandgap is 1.42 eV for the pure $FAPbI_3$, which is close but lower than other reported values from calculations (1.51 eV),[22] absorbing in the range to achieve the maximum theoretical power conversion efficiency for single-junction solar cells according to the Shockley−Queisser limit.[23] However, $FAPbI_3$ perovskite is unstable at room temperature and ambient atmosphere, transforming into a yellow powder with a hexagonal structure, identified here as 2H. For this reason, pure $FAPbI_3$ is not further analyzed in this work. The LHP's bandgap increased as Cs and Br were added to the FA-based compositions (Figure 1B). Both cation and halide substitution in $FAPbI_3$ reduces the crystal structure's lattice parameters, resulting in increased bandgap, as described and experimentally shown for the complete set of (Cs,FA) and (I,Br) compositions by An and others.[20] We observe that adding Br increases the bandgap further compared to the Cs addition. It has been demonstrated that the bandgap and lattice parameters of semiconducting materials correlate with the effective anion radius of the halides, in this case, Br.[24] Whereas the A-site cation does not participate in the band edge states, it does influence the room temperature optical properties indirectly through changes to the structure by the octahedral tilting and arrangement.[16,25] We highlight that one of the main advantages of LHPs is their property tunability through compositional engineering, as we see here on bandgap tunability when we add Cs and Br. In this case, the studied compositions have a bandgap from 1.43 to 1.58 eV, remaining in an ideal range for high-efficiency single-junction perovskite solar cells.

To study the crystal structure of these LHPs, we performed powder XRD, as shown in Figure 2. In Figure 2A, we show the structure of the perovskite phase at 300 K, corresponding to either a cubic phase of space group $Pm\bar{3}m$ (α) or a tetragonal phase of space group $P4/mbm$ (β). We analyzed in detail the XRD patterns at 300 K (Figure 2B) by Le Bail refinements (Figures S2−S4). From this initial analysis, we identified the structural phases present for each composition, as shown in Figure 2C, where α is an orange square and β is a green rectangle. All the studied compositions without Br, Cs_xBr_0, are β phase at 300 K. This structure is similar to the work by An and others,[20] where $(Cs_{17},FA_{83})PbI_3$ was tetragonal at room

https://doi.org/10.1021/acs.chemmater.4c01670
Chem. Mater. 2024, 36, 10167−10175

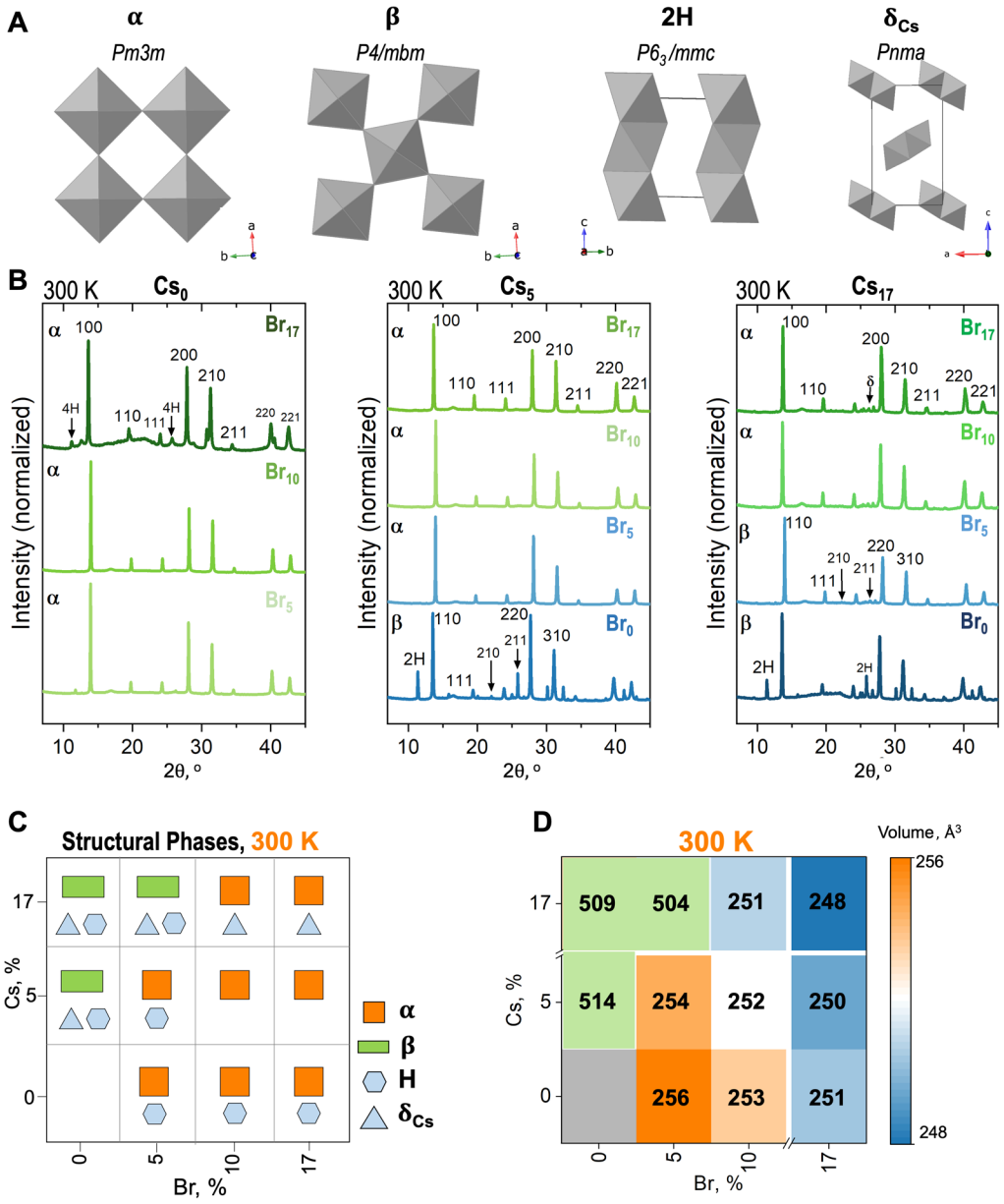

Figure 2. Crystal structure from powder XRD at 300 K. (A) Structural phases present in the $(Cs,FA)Pb(I,Br)_3$ set of compositions. (B) XRD patterns for different Cs−Br concentrations for the (Cs,FA)−(I,Br) compositions at 300 K and vacuum, (C) structural phases from Le Bail refinements, and (D) unit cell volume for the (Cs,FA)−(I,Br) compositions at 300 K. $(Cs,FA)Pb(I,Br)_3$ Temperature phase diagram.

temperature, and with the work by Charles and co-workers,[12] where $(Cs_{10}, FA_{90})PbI_3$ was tetragonal at 290 K. Adding Cs to $FAPbI_3$ structure induces a chemical pressure or lattice strain effect due to the Cs and FA cation size mismatch, leading to a structural distortion, stronger FA-iodide hydrogen bonding interaction, and symmetry breaking.[26] Therefore, the symmetry break when adding Cs explains the initial β phase for Cs_xBr_0. Adding only 5% Br to the Cs_{17} perovskite phase $(Cs_{17}Br_5)$ also results in a β structure. This low amount of Br does not change the tetragonal structure, suggesting that since there is no octahedral tilting, there are also no changes in cation rotation. However, adding more Br (10 and 17%) leads to an initially cubic perovskite structure (α) at room temperature.[5] Previous work by Johnston and co-workers showed that adding up to 15% Br to $(Cs,MA,FA)PbI_3$ suppressed the organic cation rotation, enhancing long-lived carrier lifetimes. In this case, we suggest that adding 10 or 17% of Br would similarly cause a decrease in cation rotation, leading to a higher symmetry α perovskite.

Beyond the perovskite structural analysis, we also identified secondary nonperovskite phases from the powder XRDs in Figure 2. Single-cation $CsPbI_3$ or $FAPbI_3$ form nonperovskite phases with either face- or edge-sharing octahedra. Hexagonal face-sharing $FAPbI_3$, referred to here as 2H, is a face-sharing octahedra structure with space group $P6_3/mmc$ and the orthorhombic edge-sharing $CsPbI_3$, known as δ_{Cs}, has a space group *Pnma* (Figure 2A).[27,28] There are also other intermediate hexagonal polytypes between the corner-sharing and the pure face-sharing, known as 4H or 6H.[27,29] These hexagonal polytypes (H) are present in mixed halides. Figure 2C summarizes the secondary phases at 300 K, showing the hexagonal polytypes H as hexagons and δ_{Cs} as triangles. All compositions Cs_0Br_x show some hexagonal polytypes, specifically due to their characteristic diffraction peaks between

https://doi.org/10.1021/acs.chemmater.4c01670
Chem. Mater. 2024, 36, 10167−10175

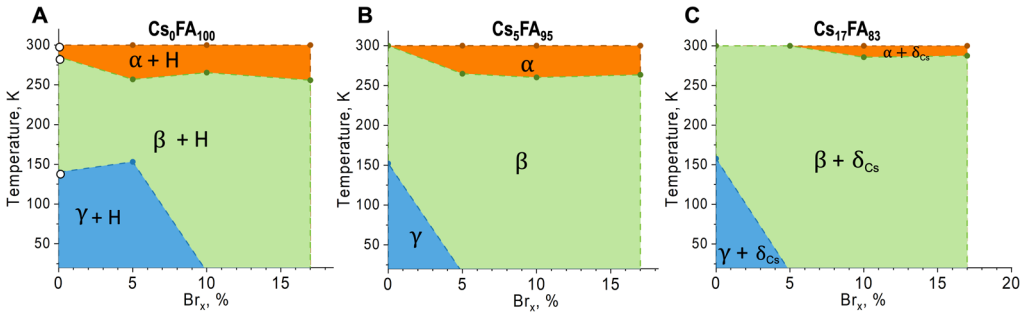

Figure 3. Composition−temperature phase diagram. Mixed-halide mixed-cation LHP in the $(Cs,FA)Pb(I,Br)_3$ compositional space. (A) Without Cs (Cs_0Br_x) as a function of Br, (B) Cs 5% (Cs_5Br_x) as a function of Br, and (C) Cs 17% ($Cs_{17}Br_x$) as a function of Br. The lines are to guide the eye and highlight different phases.

8 and 12° in 2θ of the diffraction pattern (Figure 2B). For Cs_5Br_0, we observe the formation of some nonperovskite δ_{Cs}, possibly due to phase segregation.[12] For Cs_5Br_5, some polytype H phases are observed, but remarkably, in Cs_5Br_{10} and Cs_5Br_{17}, no secondary phases are formed. The work by Gratia and others[27] shows that around 3% Cs is fundamental in FA-rich (I,Br) compositions to increase the structural chemical pressure, inhibiting the formation of polytypes, explaining why Cs is needed in (I,Br) compositions for improved stability and symmetry. Additionally, the work by Li,[13] Charles,[12] Mozur,[14] and Ghosh,[26] shows the importance of adding Cs up to 15−20% (solubility limit) since above this value, the mixed-cation LHP will phase segregate into their to phase single-cation nonperovskite phases. In the case of $Cs_{17}Br_x$, we overcome this solubility limit. Therefore, all $Cs_{17}Br_x$ compositions show the presence of the δ_{Cs} phase (Figure 2B). Herein, we see how a combination of adding less than 17% Cs and more than 5% Br (Cs_5Br_{10} and Cs_5Br_{17}), in both cases, leads to the desired combination for a single-phase high symmetry structure.

Lastly, from the powder XRD at 300 K and the Le Bail analysis, we determined the lattice parameters and calculated the unit cell volume (Figure 2D). Tetragonal structures have lattice parameters $a = b \neq c$. In the case of cubic structures, the lattice parameters are all equal: $a = b = c$. The volume for the tetragonal structure is significantly larger given that the values of a and b are around 8.96 Å, increasing the overall volume of the tetragonal unit cell. For the cubic unit cell volumes, we observe that the volume decreases as Cs and Br are added in $FAPbI_3$. Given the replacement by both smaller-size ions, the overall cubic unit cell volume is expected to decrease. A smaller sized cation, Cs^+, is replacing the larger cation FA^+ as the halide Br^- is replacing a larger ion, I^-.

To compose a low-temperature phase diagram for the (Cs,FA)−(I,Br) compositional space, we evaluated the in situ XRD of all samples by cooling the powders from 300 to 23 K in steps of 20 K (Figures S5−S7). From a general phase analysis, by plotting the diffraction pattern as a function of temperature (Figure S8), we identified the phase transition temperatures as new diffraction peaks appeared. These phase transition temperatures for all compositions are listed in Table S2. To show the overall mixed-cation and mixed-halide temperature phase diagram, we divided it into three for three Cs molar percentages, Cs_0, Cs_5, and Cs_{17} (Figure 3). Therefore, each temperature phase diagram is shown as a function of molar Br %.

First, Figure 3A shows the phase diagram for Cs_0Br_x. For Cs_0Br_0 and Cs_0Br_5, there are two low-temperature phase transitions, from α to β slightly above 250 K and from β to γ around 150 K. These two phase transitions have been reported for pure-iodide single-cation perovskites,[5−8] mixed-cation (Cs,FA),[12] and mixed-cation (MA,FA).[11,30] Generally, it is expected for the perovskite to decrease its symmetry as it is cooled, as evidenced by the tilting of the corner-sharing octahedra from cubic to tetragonal and from tetragonal to orthorhombic. These transitions are also foreseen given that as the temperature decreases, the organic cations move slower and influence the octahedra tilting due to less movement. Moreover, when increasing the Br content to Cs_0Br_{10} and Cs_0Br_{17}, we observe only one phase transition from α to β from 300 to 20 K. This represents higher stability of the tetragonal phase without the transition to orthorhombic, meaning there is less tilting of the octahedra. According to Johnston and co-workers,[31] Br incorporation, up to around 15%, suppresses cation rotation in mixed-halide perovskites at room temperature. Therefore, we can explain that the suppressed cation rotation at room temperature keeps constant down to low temperatures. With respect to secondary phases, without Cs in $FAPb(I,Br)_3$ (Cs_0Br_x), we observe the presence of hexagonal polytypes (H) in Figure S9 (explained in the previous section at 300 K).

Figure 3B shows the temperature phase diagram for $Cs_{0.05}FA_{0.95}Pb(Br_xI_{1-x})_3$ (Cs_5Br_x). For Cs_5Br_0, we observe the β phase at 300 K. We observe one phase transition from β to γ at 150 K. Adding Br, Cs_5Br_5 and Cs_5Br_{17}, leads to an initial α phase, indicating a higher perovskite symmetry at 300 K and discussed in the previous section of Figure 2. Cooling down the Cs_5Br_x perovskites leads to one phase transitions from α to β slightly above 250 K, similar to the Cs_0Br_x set. However, for all Cs_5Br_x compositions, adding Br hinders the transition from β to γ, indicating better stability of the tetragonal phase and a higher perovskite symmetry at low temperatures such as 23 K. In general, for Cs_5Br_x, no secondary phases are observed (Figures S9−S10).

Figure 3C shows the temperature phase diagram for the case of $Cs_{0.17}FA_{0.83}Pb(Br_xI_{1-x})_3$ ($Cs_{17}Br_x$). Analogous to Cs_5Br_0, without Br $Cs_{17}Br_0$, the mixed-cation perovskite adopts the tetragonal structure at 300 K. This composition shows a phase transition from β to γ at around 150 K. At 300 K, adding Br, $Cs_{17}Br_5$, retains the tetragonal perovskite structure. Remarkably, this composition shows no phase transitions in the studied range from 300 to 23 K; the β perovskite phase is stable down to very low temperatures. Increasing the Br content ($Cs_{17}Br_{10}$ and $Cs_{17}Br_{17}$) leads to an initial α perovskite phase that will then transform to β phase at around 270 K.

https://doi.org/10.1021/acs.chemmater.4c01670
Chem. Mater. 2024, 36, 10167−10175

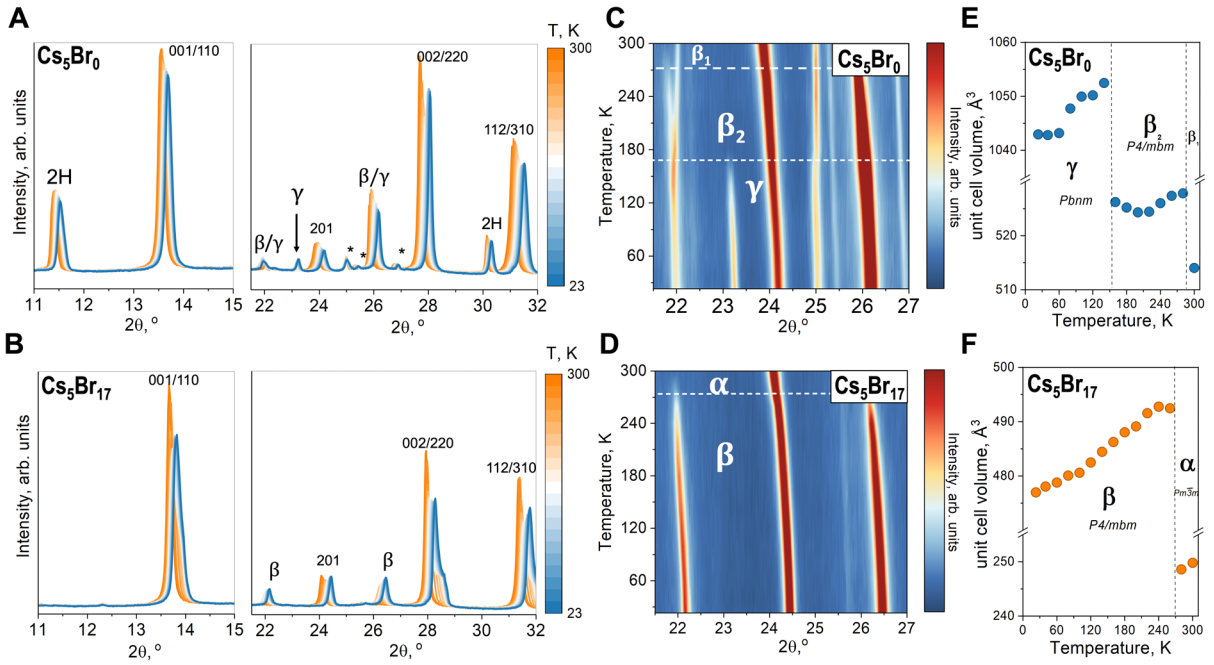

Figure 4. Effect of adding Br into the (Cs,FA)PbI_3 LHP by in situ XRD in a Cs 5% composition. (A,B) Diffraction patterns for all set of studied temperatures in two ranges of 2θ, from 11 to 15° and 21.5−32° (A) Cs_5Br_0 and (B) Cs_5Br_{17}. (C,D) Temperature versus diffraction plot from 21.5 to 27° for (C) Cs_5Br_0 and (D) Cs_5Br_{17}. (E,F) Unit cell volume as a function of temperature from Le Bail refinements for (E) Cs_5Br_0 and (F) Cs_5Br_{17}.

Equivalent to the $Cs_yFA_{1-y}Pb(Br_xI_{1-x})_3$ phase with Cs_5Br_x, for $Cs_{17}Br_x$, we observe that adding Br suppresses the phase transition from β to γ all the way down to 23 K. Therefore, adding Br improves the stability and increases the symmetry of the perovskite structure at very low temperatures. Regarding the secondary phases, all compositions with $Cs_{17}Br_x$ show a minor peak corresponding to the nonperovskite δ_{Cs} (Figure S10) due to phase segregation since it overpasses the solubility limit.[12] It is known that this nonperovskite is photoinactive and unwanted for solar cell applications.[4]

Br Addition Improves Stability at Low Temperatures. We evaluated the low-temperature phase transitions for a mixed-cation (Cs,FA) and mixed-halide (I,Br) perovskite, as shown in Figure 1A. In Figure 3, we presented the three phase diagrams to compare different ratios of mixed-cation (Cs,FA) and mixed-halide (I,Br). These phase diagrams reveal that the addition of Br to mixed-cation (Cs,FA) compositions stabilizes the perovskite β phase over a wide temperature range, from approximately 260 K down to 23 K. This stabilization prevents significant structural changes, symmetry variations, and octahedral tilting that occur in the γ phase.[32] Figure 4 illustrates the in situ XRD pattern and results for two compositions, Cs_5Br_0 and Cs_5Br_{17}. The complete set of temperature-dependent diffraction patterns can be found in Figures S5−S8. Figure 4A,B shows two significant diffraction regions for the (A) Cs_5Br_{10} and (B) Cs_5Br_{17} powders as the samples are cooled from 300 K (orange) to 23 K (blue). The main perovskite Bragg peaks are highlighted, and the Bragg peaks correspond to nonperovskite 2H and δ_{Cs} phases are shown. Figure 4C,D shows the diffraction regions from 21.5 to 27° as a function of temperature for (C) Cs_5Br_0 and (D) Cs_5Br_{17}. For Cs_5Br_0 in Figure 4C, the perovskite phase starts as β at 300 K, with characteristic peaks around 22 and 26.5° corresponding to the 210 and 211 Bragg peaks of the tetragonal phase. For Cs_5Br_0, a new peak appears around 23.2° at 167 K, indicating the presence of the γ phase. In contrast, Figure 4D shows that for Cs_5Br_{17}, the perovskite phase initially adopts the α structure. As the temperature decreases, Bragg peaks of the β phase appear at ~267 K, and no peak related to the γ phase is observed down to 23 K. Furthermore, Cs_5Br_{17} does not exhibit any diffraction peaks attributed to secondary phases, maintaining a single perovskite phase structure from 300 to 23 K. For further analysis, from Le Bail refinements, we obtained the unit cell's lattice parameters (Tables S3 and S4 and Figures S11 and S12) and the unit cell volume (Figures 4E,F). Figure 4E shows the unit cell volume as a function of temperature for a composition without Br, Cs_5Br_0. We observed a significant increase in volume from 300 to 280 K. However, in both cases, it fits a tetragonal structure of the space group *P*4/*mbm*. After the initial increase, the volume decreases as temperature decreases, as expected.[9] Below 160 K, the perovskite phase transforms into the γ phase with space group *Pbnm*. Therefore, the unit cell volume increases and then keeps decreasing as a function of temperature. When Br is added (Cs_5Br_{17}), Figure 4F shows the unit cell volume as a function of temperature, evidencing the phase transition from α to β. For the β phase, there is a linear decrease of the unit cell volume as a function of temperature down to 23 K.

The observed phase transitions and structural behavior in mixed-cation mixed-halide perovskites differ from those reported in single-cation or single-halide systems. Adding Br to single-cation iodide compositions, such as $MAPb(I,Br)_3$[9] or $CsPb(I,Br)_3$,[10] has resulted in a transition from the β to the γ phase. Similarly, in mixed-cation and single-halide systems, such as (Cs,FA)PbI_3, the transition to the γ phase has been reported in the range of miscibility.[5] Remarkably, in (Cs,FA)-$PbBr_3$, Cs substitution has been shown to suppress phase transitions at lower temperatures.[14] Mozur et al. attributed this phase stability to local compressive strain caused by Cs

https://doi.org/10.1021/acs.chemmater.4c01670
Chem. Mater. 2024, 36, 10167−10175

substitution, overriding the orientation driven by the organic−organic interactions and disrupting changes in low-temperature phase transitions. They highlighted the sensitivity of organic−organic interactions in $FAPbBr_3$, explaining the advantages of Cs incorporation in halide perovskites. Other studies have also reported the suppression of phase transitions by incorporating Cs in $MAPbBr_3$, attributed to compressive chemical pressure.[32] Similarly, Ray et al. suppressed the orthorhombic phase of $MAPbBr_3$ by adding DMA and forming a mixed-cation $(MA,DMA)PbBr_3$ perovskite.[16] This suppression was attributed to increased disorder of organic cations and a less distorted inorganic framework.[33] Building upon this understanding, we suggest that the addition of Cs and Br to the $FAPbI_3$ perovskite, forming a $(Cs,FA)Pb(I,Br)_3$ framework, compresses the structure, as evidenced by smaller lattice parameters, affecting the interactions between organic cations and increasing disorder.

To evaluate the effect of crystal structure variations in the electrical properties of $(Cs,FA)Pb(I,Br)_3$ perovskites, we deposited perovskite thin films for 6 selected compositions and used them to fabricate and evaluate the performance of solar cells (Figure S13). In general, by analyzing the crystal structure of the perovskite films using room temperature XRD (Figure S13A), the thin film samples without Cs (Cs_0Br_x) or Cs_5Br_x did not show the same perovskite or nonperovskite phases as the powder samples (Figure 2). We attribute this inconsistency to different thin film deposition parameters, such as solvent and antisolvent, which play a critical role in the crystallization kinetics and phase formation of the metastable perovskite.[34] Nonperovskite hexagonal phases are detrimental to solar cell performance in $FAPbI_3$-based compositions.[35,36] Therefore, the composition that showed the minimum power conversion efficiency in solar cells was Cs_0Br_{17} (Figure S13B), partially due to hexagonal secondary phases (Figure S13A). Cs_5Br_{17} also showed a low-performance solar cell and the presence of nonperovskite phases. The best power conversion efficiency of solar cells was the composition $Cs_{17}Br_{10}$, correlated to a single-phase perovskite.

To evaluate the charge carrier transport properties, we chose two perovskite thin film compositions with the same crystal structure as their powder samples, one without Br ($Cs_{17}Br_0$) and one without $Cs_{17}Br_{17}$ (Figure S14). We used time-resolved THz spectroscopy to measure the charge carrier mobility as a function of temperature for $Cs_{17}Br_0$ and $Cs_{17}Br_{17}$, as shown in Figure S5 (methods in the Supporting Information). Consistent with literature reports where higher Br content leads to lower carrier mobility, the carrier mobility for $Cs_{17}Br_{17}$ is lower than that for $Cs_{17}Br_0$ at all temperatures.[3,37] We observed that the carrier mobility increases for both compositions as the temperature decreased from 300 to 100 K. The increase in carrier mobility is expected given that lower phonon vibrations at lower temperatures improve carrier transport.[38] We observe a small discontinuity in the mobility data, in contrast to other reports where no significant discontinuities across structural phase transitions were observed.[38] For the film without Br ($Cs_{17}Br_0$) in Figure 5A, we observe a slope change corresponding to a phase transition at around 175 K, which we attribute to a crystal phase transition from β to γ, close to the powder phase transition temperature in Figures 3C and S8. Similarly, when adding Br ($Cs_{17}Br_{17}$), Figure 5B shows the phase transition from α to β at around 270 K, close to the phase transition observed by in situ XRD (Figures 3C and S8). The increase in mobility for both

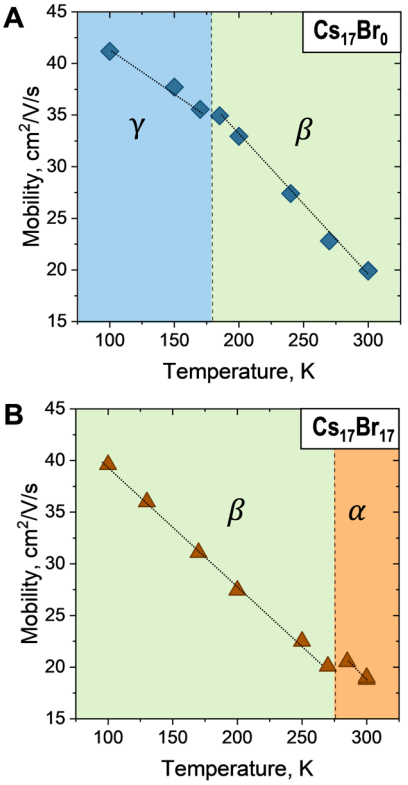

Figure 5. Carrier mobility as a function of temperature. (A) Without Br $Cs_{17}Br_0$ and (B) with Br $Cs_{17}Br_{17}$. Lines are to guide the eye and highlight discontinuity across phase transition temperatures.

samples at lower temperatures is modest because we average the mobility values across different excited carrier densities (Figures S15 and S16). At higher excitation fluences, carrier−carrier scattering dominates the carrier mobility rather than phonon scattering. By examining the average carrier mobility at both high and low excitation fluences, the impact on carrier transport due to the structural phase transition is visible and not masked by temperature-dependent phonon scattering.[39] Overall, the carrier mobilities of the two samples across the temperature range probed are very similar, supporting that the crystal symmetry is not the dominant factor in determining carrier transport in perovskite materials.[39]

CONCLUSIONS

In conclusion, this work shows for the first time the low-temperature phase transitions for a mixed-cation and mixed-halide perovskite. We measured in situ powder XRD to create temperature phase diagrams for different concentrations of Cs and Br in $(Cs,FA)Pb(I,Br)_3$ perovskites. By replacing I with Br in (Cs,FA) compositions, we found that the transition from a tetragonal to orthorhombic phase at low temperatures (below 150 K) was suppressed, resulting in a more symmetrical perovskite structure with potential applications in low-temperature settings. When Cs was not present, we observed the formation of nonperovskite hexagonal phases. However, the addition of Cs and Br prevented the formation of hexagonal structures. It is important to note that the inclusion of 17% Cs resulted in the formation of the secondary nonperovskite orthorhombic δ-$CsPbI_3$ phase. From these findings, it can be concluded that adding Br to (Cs,FA) perovskites enhances the stability of the β phase over a wider

https://doi.org/10.1021/acs.chemmater.4c01670
Chem. Mater. 2024, 36, 10167−10175

temperature range, which is advantageous for low-temperature applications. Although the introduction of Br increases the bandgap of the perovskite, which reduces the number of absorbed photons, the overall crystal structure becomes more robust and contributes to long-term stability. To gain a comprehensive understanding of how the crystal structure behaves across the entire temperature range, further investigations focusing on the fundamental structural aspects are essential.

METHODOLOGY

Experimental Section. *Mixed-Cation Mixed-Halide (Cs,FA)Pb(I,Br)$_3$ Precursor Solution.* Mixed-cation and mixed-halide $Cs_yFA_{1-y}Pb(I_xBr_{1-x})_3$ perovskites were prepared with different molar ratios of Cs/FA (y) and Br/I (x). The precursor powders used were CsI (Sigma), FAI (TCI), PbI_2 (TCI), and $PbBr_2$ (TCI). The precursor powders were weighted on the same vial to form a 0.5 M solution in a mixed solvent of gamma-butyrolactone (GBL) and dimethylformamide (DMF) with a volume ratio of 2:1. The precursor solution was mixed at 600 rpm and 60 °C for 1 h. The solutions were stoichiometric A/Pb (1:1).

Powder Synthesis. After the precursor solution was mixed, it was evaporated at 170 °C for 40 min on a glass Petri dish. A solid was formed on the Petri dish, which was broken into pieces with a spatula and left sintering on the hot plate at 170 °C for 1 h. Afterward, this solid was completely removed and ground into a very fine powder with a mortar.

Characterization. *UV−vis.* We measured UV−vis absorption spectroscopy using the PerkinElmer UV/vis, NIR Spectrometer Lambda 750 S, at the Helmholtz Zentrum Berlin (HZB). The spectrometer has a double-beam, double-monochromator, ratio-recording optical system. The instrument has a Praying Mantis Diffuse Reflection accessory in the sample compartment and a 100 mm integrating sphere accessory in the detector. This instrument is suitable for the measurement of powders.

In Situ Powder XRD. For the set of powder LHPs mixed-cations and mixed-halides, the temperature-dependent phase transitions were measured by in situ XRD. Synchrotron-based in situ XRD was measured at beamline KMC-2 in BESSY II at the HZB, Germany. The instrument used a Bruker Vantec 2000 area detector. The X-rays had an energy of 8 keV optimized for the beamline. For the temperature controller, a closed cycle refrigerator of the reference TMP-CCR-HXR was used. XRD patterns were taken from 300 to 20 K in steps of 20 K. This beamline offered both the experimental precision as well as the sample environment to perform such investigations. Powder studies were also important for a better indication of the thermodynamic processes due to a more pronounced crystallization process, less exposed surfaces, a larger probed volume compared to thin film samples, and better instrumental resolution. Le Bail fittings using the FullProf software were done to calculate the lattice parameters and phase refinement for the samples at 300 K.

Temperature-Dependent Carrier Mobility. Charge carrier transport was characterized by using time-resolved THz spectroscopy. Details of the setup can be found in,[40] with the important parameters described briefly here. The perovskite samples deposited on double-side-polished z-cut quartz substrates were excited by a femtosecond laser pulse with the wavelength centered at 400 nm, focusing to an area with a diameter of 2 mm. The carrier transport properties were measured using a subpicosecond THz pulse focused onto the center 1 mm diameter spot of the excited area. The THz transmission amplitude was recorded using an electro-optic sampling technique and a lock-in amplifier.[41] Free mobile charge carriers attenuate THz probe pulses, and the transmission reduction was proportional to the photoconductivity of the sample. The samples were loaded into a continuous-flow cryostat (Janice ST-100H) with z-cut quartz windows for transparency in the THz frequency range. Samples were loaded in the vacuum chamber and cooled to liquid nitrogen temperature first, and the measurements were conducted on the heating cycle between 100 and 300 K. At each temperature, samples were excited at three excitation densities, corresponding to laser fluences of 30, 90, and 140 $\mu J/cm^2$. After excitation at the highest laser fluence, repeated measurements at a low fluence ensured that there was no sample degradation. Room temperature measurements were conducted before the temperature cycle for comparison to the room temperature measurement at the end of the experiment to ensure that no sample degradation occurred during the measurement. The reported carrier mobility was the average mobility measured with the three excited fluences.

ASSOCIATED CONTENT

Supporting Information

The Supporting Information is available free of charge at https://pubs.acs.org/doi/10.1021/acs.chemmater.4c01670.

> UV−vis spectra; Le Bail refinements and lattice parameters at 300 K; complete XRD patterns for all compositions at all temperatures; in situ temperature XRD 2D maps for all compositions; phase transformation temperatures for all compositions; lattice parameter values for volume calculations; perovskite thin films XRD; solar cell measurements and statistics; thin films XRD used for THz conductivity measurements; and raw transient THz conductivity data (PDF)

AUTHOR INFORMATION

Corresponding Authors

Susan Schorr − *Department Structure and Dynamics of Energy Materials, Helmholtz-Zentrum Berlin Für Materialien und Energie, Berlin 14109, Germany; Freie Universitaet Berlin, Institute of Geological Sciences, Berlin 12249, Germany*; Email: susan.schorr@helmholtz-berlin.de

Juan-Pablo Correa-Baena − *School of Materials Science and Engineering, Georgia Institute of Technology, Atlanta, Georgia 30332, United States*; orcid.org/0000-0002-3860-1149; Email: jpcorrea@gatech.edu

Authors

Juanita Hidalgo − *School of Materials Science and Engineering, Georgia Institute of Technology, Atlanta, Georgia 30332, United States; Department Structure and Dynamics of Energy Materials, Helmholtz-Zentrum Berlin Für Materialien und Energie, Berlin 14109, Germany*; orcid.org/0000-0002-5832-3262

Joachim Breternitz − *Department Structure and Dynamics of Energy Materials, Helmholtz-Zentrum Berlin Für Materialien und Energie, Berlin 14109, Germany*; orcid.org/0000-0002-0192-6919

https://doi.org/10.1021/acs.chemmater.4c01670
Chem. Mater. 2024, 36, 10167−10175

Daniel M. Többens − *Department Structure and Dynamics of Energy Materials, Helmholtz-Zentrum Berlin Für Materialien und Energie, Berlin 14109, Germany*
Diana K. LaFollette − *School of Materials Science and Engineering, Georgia Institute of Technology, Atlanta, Georgia 30332, United States*
Charles N. B. Pedorella − *Department of Physics, Wesleyan University, Middletown, Connecticut 06459, United States*
Meng-Ju Sher − *Department of Physics, Wesleyan University, Middletown, Connecticut 06459, United States;* orcid.org/0000-0003-1044-5559

Complete contact information is available at: https://pubs.acs.org/10.1021/acs.chemmater.4c01670

Author Contributions

J.H. designed the project, wrote the manuscript, synthesized all powder samples, characterized powder XRD and UV−vis, did all the Le Bail refinements, fabricated the solar cells, and analyzed all data. All powder samples were synthesized and characterized at HZB, under the supervision, guidance, and help in the analysis from J.B. and S.S. D.T. helped in the in situ XRD experiments at BESSY II and contributed to data analysis. D.K.L. fabricated and measured XRD and analyzed all thin films. C.N.B. measured THz under the supervision and analysis of M.J.S. J.P.C.B. and S.S supervised the entire work. All the authors have read, corrected, and agreed with the manuscript.

Notes

The authors declare no competing financial interest.

■ ACKNOWLEDGMENTS

All authors thank the Helmoltz-Zentrum Berlin für Materialien und Energie for the allocation of synchrotron radiation beamtime at the KMC-II Diffraction beamline at BESSY II (ST- 221-11048). J.H. acknowledges the DAAD German Academic Exchange one year grant (2021-2022) and the Graduate Education for Minorities (GEM) fellowship for the year of project funding. D.K.L. acknowledges the NSF-GRF DGE-2039655 funding. M.J.S. and C.N.B acknowledge the NSF DMR 2316827 funding. Any findings and conclusions are those of the author(s) and do not necessarily reflect the views of the National Science Foundation.

■ REFERENCES

(1) Saliba, M.; Matsui, T.; Seo, J.-Y.; Domanski, K.; Correa-Baena, J.-P.; Nazeeruddin, M. K.; Zakeeruddin, S. M.; Tress, W.; Abate, A.; Hagfeldt, A.; Grätzel, M. Cesium-Containing Triple Cation Perovskite Solar Cells: Improved Stability, Reproducibility and High Efficiency. *Energy Environ. Sci.* **2016**, *9* (6), 1989−1997.
(2) Eperon, G. E.; Stranks, S. D.; Menelaou, C.; Johnston, M. B.; Herz, L. M.; Snaith, H. J. Formamidinium Lead Trihalide: A Broadly Tunable Perovskite for Efficient Planar Heterojunction Solar Cells. *Energy Environ. Sci.* **2014**, *7* (3), 982.
(3) Rehman, W.; McMeekin, D. P.; Patel, J. B.; Milot, R. L.; Johnston, M. B.; Snaith, H. J.; Herz, L. M. Photovoltaic Mixed-Cation Lead Mixed-Halide Perovskites: Links between Crystallinity, Photo-Stability and Electronic Properties. *Energy Environ. Sci.* **2017**, *10* (1), 361−369.
(4) An, Y.; Hidalgo, J.; Perini, C. A. R.; Castro-Méndez, A. F.; Vagott, J. N.; Bairley, K.; Wang, S.; Li, X.; Correa-Baena, J.-P. Structural Stability of Formamidinium- and Cesium-Based Halide Perovskites. *ACS Energy Lett.* **2021**, *6* (5), 1942−1969.
(5) Weber, O. J.; Ghosh, D.; Gaines, S.; Henry, P. F.; Walker, A. B.; Islam, M. S.; Weller, M. T. Phase Behavior and Polymorphism of Formamidinium Lead Iodide. *Chem. Mater.* **2018**, *30* (11), 3768−3778.
(6) Steele, J. A.; Jin, H.; Dovgaliuk, I.; Berger, R. F.; Braeckevelt, T.; Yuan, H.; Martin, C.; Solano, E.; Lejaeghere, K.; Rogge, S. M. J.; Notebaert, C.; Vandezande, W.; Janssen, K. P. F.; Goderis, B.; Debroye, E.; Wang, Y.-K.; Dong, Y.; Ma, D.; Saidaminov, M.; Tan, H.; Lu, Z.; Dyadkin, V.; Chernyshov, D.; Van Speybroeck, V.; Sargent, E. H.; Hofkens, J.; Roeffaers, M. B. J. Thermal Unequilibrium of Strained Black $CsPbI_3$ Thin Films. *Science* **2019**, *365* (6454), 679−684.
(7) Franz, A.; Többens, D. M.; Lehmann, F.; Kärgell, M.; Schorr, S. The Influence of Deuteration on the Crystal Structure of Hybrid Halide Perovskites: A Temperature-Dependent Neutron Diffraction Study of $FAPbBr_3$. *Acta Crystallogr., Sect. B: Struct. Sci., Cryst. Eng. Mater.* **2020**, *76* (2), 267−274.
(8) Songvilay, M.; Giles-Donovan, N.; Bari, M.; Ye, Z.-G.; Minns, J. L.; Green, M. A.; Xu, G.; Gehring, P. M.; Schmalzl, K.; Ratcliff, W. D.; Brown, C. M.; Chernyshov, D.; Van Beek, W.; Cochran, S.; Stock, C. Common Acoustic Phonon Lifetimes in Inorganic and Hybrid Lead Halide Perovskites. *Phys. Rev. Mater.* **2019**, *3* (9), 093602.
(9) Lehmann, F.; Franz, A.; Többens, D.; Levcenco, S.; Unold, T.; Taubert, A.; Schorr, S. The Phase Diagram of a Mixed Halide (Br, I) Hybrid Perovskite Obtained by Synchrotron X-Ray Diffraction. *RSC Adv.* **2019**, *9* (20), 11151−11159.
(10) Näsström, H.; Becker, P.; Márquez, J. A.; Shargaieva, O.; Mainz, R.; Unger, E.; Unold, T. Dependence of Phase Transitions on Halide Ratio in Inorganic $CsPb(Br_xI_{1-x})_3$ Perovskite Thin Films Obtained from High-Throughput Experimentation. *J. Mater. Chem. A* **2020**, *8* (43), 22626−22631.
(11) Francisco-López, A.; Charles, B.; Alonso, M. I.; Garriga, M.; Campoy-Quiles, M.; Weller, M. T.; Goñi, A. R. Phase Diagram of Methylammonium/Formamidinium Lead Iodide Perovskite Solid Solutions from Temperature-Dependent Photoluminescence and Raman Spectroscopies. *J. Phys. Chem. C* **2020**, *124* (6), 3448−3458.
(12) Charles, B.; Weller, M. T.; Rieger, S.; Hatcher, L. E.; Henry, P. F.; Feldmann, J.; Wolverson, D.; Wilson, C. C. Phase Behavior and Substitution Limit of Mixed Cesium-Formamidinium Lead Triiodide Perovskites. *Chem. Mater.* **2020**, *32* (6), 2282−2291.
(13) Li, Z.; Yang, M.; Park, J.-S.; Wei, S.-H.; Berry, J. J.; Zhu, K. Stabilizing Perovskite Structures by Tuning Tolerance Factor: Formation of Formamidinium and Cesium Lead Iodide Solid-State Alloys. *Chem. Mater.* **2016**, *28* (1), 284−292.
(14) Mozur, E. M.; Hope, M. A.; Trowbridge, J. C.; Halat, D. M.; Daemen, L. L.; Maughan, A. E.; Prisk, T. R.; Grey, C. P.; Neilson, J. R. Cesium Substitution Disrupts Concerted Cation Dynamics in Formamidinium Hybrid Perovskites. *Chem. Mater.* **2020**, *32* (14), 6266−6277.
(15) Simenas, M.; Balciunas, S.; Wilson, J. N.; Svirskas, S.; Kinka, M.; Garbaras, A.; Kalendra, V.; Gagor, A.; Szewczyk, D.; Sieradzki, A.; Maczka, M.; Samulionis, V.; Walsh, A.; Grigalaitis, R.; Banys, J. Suppression of Phase Transitions and Glass Phase Signatures in Mixed Cation Halide Perovskites. *Nat. Commun.* **2020**, *11* (1), 5103.
(16) Ray, A.; Martín-García, B.; Moliterni, A.; Casati, N.; Boopathi, K. M.; Spirito, D.; Goldoni, L.; Prato, M.; Giacobbe, C.; Giannini, C.; Di Stasio, F.; Krahne, R.; Manna, L.; Abdelhady, A. L. Mixed Dimethylammonium/Methylammonium Lead Halide Perovskite Crystals for Improved Structural Stability and Enhanced Photo-detection. *Adv. Mater.* **2022**, *34* (7), 2106160.
(17) Hui, W.; Chao, L.; Lu, H.; Xia, F.; Wei, Q.; Su, Z.; Niu, T.; Tao, L.; Du, B.; Li, D.; Wang, Y.; Dong, H.; Zuo, S.; Li, B.; Shi, W.; Ran, X.; Li, P.; Zhang, H.; Wu, Z.; Ran, C.; Song, L.; Xing, G.; Gao, X.; Zhang, J.; Xia, Y.; Chen, Y.; Huang, W. Stabilizing Black-Phase Formamidinium Perovskite Formation at Room Temperature and High Humidity. *Science* **2021**, *371* (6536), 1359−1364.
(18) Lee, J.-W.; Kim, D.-H.; Kim, H.-S.; Seo, S.-W.; Cho, S. M.; Park, N.-G. Formamidinium and Cesium Hybridization for Photo- and Moisture-Stable Perovskite Solar Cell. *Adv. Energy Mater.* **2015**, *5* (20), 1501310.
(19) Yi, C.; Luo, J.; Meloni, S.; Boziki, A.; Ashari-Astani, N.; Grätzel, C.; Zakeeruddin, S. M.; Röthlisberger, U.; Grätzel, M. Entropic

Stabilization of Mixed A-Cation ABX $_3$ Metal Halide Perovskites for High Performance Perovskite Solar Cells. *Energy Environ. Sci.* **2016**, *9* (2), 656−662.
(20) An, Y.; Perini, C. A. R.; Hidalgo, J.; Castro-Méndez, A. F.; Vagott, J. N.; Li, R.; Saidi, W. A.; Wang, S.; Li, X.; Correa-Baena, J.-P. Identifying High-Performance and Durable Methylammonium-Free Lead Halide Perovskites *via* High-Throughput Synthesis and Characterization. *Energy Environ. Sci.* **2021**, *14* (12), 6638−6654.
(21) Makuła, P.; Pacia, M.; Macyk, W. How To Correctly Determine the Band Gap Energy of Modified Semiconductor Photocatalysts Based on UV−Vis Spectra. *J. Phys. Chem. Lett.* **2018**, *9* (23), 6814−6817.
(22) Tao, S.; Schmidt, I.; Brocks, G.; Jiang, J.; Tranca, I.; Meerholz, K.; Olthof, S. Absolute Energy Level Positions in Tin- and Lead-Based Halide Perovskites. *Nat. Commun.* **2019**, *10* (1), 2560.
(23) Tress, W. Maximum Efficiency and Open-Circuit Voltage of Perovskite Solar Cells. In *Organic-Inorganic Halide Perovskite Photovoltaics: From Fundamentals to Device Architectures*; Springer: Switzerland, 2016.
(24) Unger, E. L.; Kegelmann, L.; Suchan, K.; Sörell, D.; Korte, L.; Albrecht, S. Roadmap and Roadblocks for the Band Gap Tunability of Metal Halide Perovskites. *J. Mater. Chem. A* **2017**, *5* (23), 11401−11409.
(25) Amat, A.; Mosconi, E.; Ronca, E.; Quarti, C.; Umari, P.; Nazeeruddin, Md. K.; Grätzel, M.; De Angelis, F. Cation-Induced Band-Gap Tuning in Organohalide Perovskites: Interplay of Spin−Orbit Coupling and Octahedra Tilting. *Nano Lett.* **2014**, *14* (6), 3608−3616.
(26) Ghosh, D.; Smith, A. R.; Walker, A. B.; Islam, M. S. Mixed A-Cation Perovskites for Solar Cells: Atomic-Scale Insights Into Structural Distortion, Hydrogen Bonding, and Electronic Properties. *Chem. Mater.* **2018**, *30* (15), 5194−5204.
(27) Gratia, P.; Zimmermann, I.; Schouwink, P.; Yum, J.-H.; Audinot, J.-N.; Sivula, K.; Wirtz, T.; Nazeeruddin, M. K. The Many Faces of Mixed Ion Perovskites: Unraveling and Understanding the Crystallization Process. *ACS Energy Lett.* **2017**, *2* (12), 2686−2693.
(28) Dastidar, S.; Hawley, C. J.; Dillon, A. D.; Gutierrez-Perez, A. D.; Spanier, J. E.; Fafarman, A. T. Quantitative Phase-Change Thermodynamics and Metastability of Perovskite-Phase Cesium Lead Iodide. *J. Phys. Chem. Lett.* **2017**, *8* (6), 1278−1282.
(29) Li, Z.; Park, J.-S.; Walsh, A. Evolutionary Exploration of Polytypism in Lead Halide Perovskites. *Chem. Sci.* **2021**, *12* (36), 12165−12173.
(30) Šimėnas, M.; Balčiūnas, S.; Svirskas, Š.; Kinka, M.; Ptak, M.; Kalendra, V.; Gągor, A.; Szewczyk, D.; Sieradzki, A.; Grigalaitis, R.; Walsh, A.; Mączka, M.; Banys, J. Phase Diagram and Cation Dynamics of Mixed $MA_xFA_xPbBr_3$ Hybrid Perovskites. *Chem. Mater.* **2021**, *33* (15), 5926−5934.
(31) Johnston, A.; Walters, G.; Saidaminov, M. I.; Huang, Z.; Bertens, K.; Jalarvo, N.; Sargent, E. H. Bromine Incorporation and Suppressed Cation Rotation in Mixed-Halide Perovskites. *ACS Nano* **2020**, *14* (11), 15107−15118.
(32) Mozur, E. M.; Maughan, A. E.; Cheng, Y.; Huq, A.; Jalarvo, N.; Daemen, L. L.; Neilson, J. R. Orientational Glass Formation in Substituted Hybrid Perovskites. *Chem. Mater.* **2017**, *29* (23), 10168−10177.
(33) Yang, B.; Ming, W.; Du, M.-H.; Keum, J. K.; Puretzky, A. A.; Rouleau, C. M.; Huang, J.; Geohegan, D. B.; Wang, X.; Xiao, K. Real-Time Observation of Order-Disorder Transformation of Organic Cations Induced Phase Transition and Anomalous Photoluminescence in Hybrid Perovskites. *Adv. Mater.* **2018**, *30* (22), 1705801.
(34) Ke, L.; Luo, S.; Ren, X.; Yuan, Y. Factors Influencing the Nucleation and Crystal Growth of Solution-Processed Organic Lead Halide Perovskites: A Review. *J. Phys. D: Appl. Phys.* **2021**, *54* (16), 163001.
(35) Hidalgo, J.; Kaiser, W.; An, Y.; Li, R.; Oh, Z.; Castro-Méndez, A. F.; LaFollette, D. K.; Kim, S.; Lai, B.; Breternitz, J.; Schorr, S.; Perini, C. A. R.; Mosconi, E.; De Angelis, F.; Correa-Baena, J.-P. Synergistic Role of Water and Oxygen Leads to Degradation in Formamidinium-Based Halide Perovskites. *J. Am. Chem. Soc.* **2023**, *145* (45), 24549−24557.
(36) Hidalgo, J.; Atourki, L.; Li, R.; Castro-Méndez, A. F.; Kim, S.; Sherman, E. A.; Bieber, A. S.; Sher, M.; Nienhaus, L.; Perini, C. A. R.; Correa-Baena, J.-P. Bulky Cation Hinders Undesired Secondary Phases in FAPbI3 Perovskite Solar Cells. *Mater. Today* **2023**, *68*, 13−21.
(37) Rehman, W.; Milot, R. L.; Eperon, G. E.; Wehrenfennig, C.; Boland, J. L.; Snaith, H. J.; Johnston, M. B.; Herz, L. M. Charge-Carrier Dynamics and Mobilities in Formamidinium Lead Mixed-Halide Perovskites. *Adv. Mater.* **2015**, *27* (48), 7938−7944.
(38) Milot, R. L.; Eperon, G. E.; Snaith, H. J.; Johnston, M. B.; Herz, L. M. Temperature-Dependent Charge-Carrier Dynamics in CH3NH3PbI3 Perovskite Thin Films. *Adv. Funct. Mater.* **2015**, *25* (39), 6218−6227.
(39) Herz, L. M. Charge-Carrier Mobilities in Metal Halide Perovskites: Fundamental Mechanisms and Limits. *ACS Energy Lett.* **2017**, *2* (7), 1539−1548.
(40) Erodici, M. P.; Pierone, P. J.; Hartono, N. T. P.; Hidalgo, J.; Lai, B.; Buonassisi, T.; Correa-Baena, J.-P.; Sher, M.-J. Enhanced Charge Carrier Lifetime and Mobility as a Result of Rb and Cs Incorporation in Hybrid Perovskite. *Appl. Phys. Lett.* **2021**, *118* (6), 063901.
(41) Hegmann, F. A.; Ostroverkhova, O.; Cooke, D. G. Probing Organic Semiconductors with Terahertz Pulses. In *Photophysics of Molecular Materials*; John Wiley & Sons, Ltd, 2005; pp 367−428.

https://doi.org/10.1021/acs.chemmater.4c01670
Chem. Mater. 2024, 36, 10167−10175